Cement and Concrete Composites 167 (2026) 106452

Contents lists available at ScienceDirect

Cement and Concrete Composites

journal homepage: www.elsevier.com/locate/cemconcomp

Rheological control of cementitious composites incorporating ceramic wastes for 3D printing applications

Lucia Ferrari [a,*], Giacomo Rizzieri [b], Liberato Ferrara [b], Elisa Franzoni [a]

[a] Department of Civil, Chemical, Environmental, and Materials Engineering (DICAM), University of Bologna - Via Terracini 28, 40131, Bologna, Italy
[b] Department of Civil and Environmental Engineering, Polytechnic of Milan - Piazza Leonardo da Vinci 32, 20133, Milano, Italy

ARTICLE INFO

Keywords:
Ceramic waste
Recycling
Limestone calcined clay cement
Rheology
3D printing
Numerical simulations

ABSTRACT

In response to the environmental impact of cement production and industrial discarded materials, this study explores the valorisation of ceramic wastes as replacement of clinker in low-carbon cementitious composites for application in additive manufacturing. Ceramic wastes from different sources were used as substitute of calcined clay in limestone calcined clay cement (LC3) mortar. The embodied CO_2 reduction of these new binders exceeds 40 % compared to Portland Cement (PC), thus representing a notable advancement in low-emission cementitious composites. The influence of six ceramic wastes on the fresh state performance of mortar was assessed through flow table tests and rheological measurements. A ball measuring system was used to assess viscosity, static yield stress, and their early-age evolution, combining the high resolution of benchtop rheometers with the possibility of testing of 3D-printable mortars with aggregates up to 2 mm, featuring high yield stress values. Numerical simulations based on the Particle Finite Element Method were then used to evaluate the printability of developed mix designs, avoiding time consuming trial and error testing campaigns and paving the way for through printing trials on a selected set of waste materials.

Numerical simulations highlighted that, while all tested formulations showed good performance for small-scale 3D printing, careful material selection becomes crucial when targeting larger structures to ensure stability and minimize deformation. Additionally, the simulations allowed prediction of material behaviour, particularly valuable given the high variability of waste-based constituents, emphasizing the innovative combination of circular economy concepts with a unique approach to additive manufacturing supported by numerical simulations.

1. Introduction

The cement industry is one of the largest contributors to global CO_2 emissions, accounting for about 7 % of the total [1], primarily due to clinker production, which requires high-temperature process and releases large amounts of CO_2 during calcination of limestone. In response, innovative strategies are presently explored to reduce these emissions, including the use of alternative binders [2], supplementary cementitious materials (SCMs) [3,4], and carbon capture, utilization and storage technologies [5,6]. On one side, Limestone Calcined Clay Cement (LC3) has emerged as a promising low-carbon alternative, offering up to 40 % embodied CO_2 reduction compared to Portland Cement (PC) [7]. This binder ensures adequate mechanical strength [8] by refining the pore structure [9], also contributing to durability enhancement [10–13] and offering positive synergies even when used with recycled aggregates [14,15]. On the other side, among many industrial by-products and discarded materials with potential as SCMs, ceramic waste remains underutilized despite its high pozzolanic potential [16,17]. In Europe alone, tile manufacturing generates approximately 3 million tons of ceramic waste annually, about 35 % of which is not recycled and often ends up in landfills [18,19]. This waste, originating from the production of tiles, sanitaryware, and refractories, has high silica and alumina content, making it suitable for use in cement formulations [20,21]. Replacing calcined clay with ceramic waste in LC3 formulation can reduce embodied CO_2 emissions by over 40 % compared to PC. However, research on this approach remains limited [22]. Moreover, ceramic waste as a substitute of calcined clay has the potential of improving the rheological behaviour of LC3, that still stands as one of the biggest challenges in the use of this material [23], for which achieving target workability requires high dosages and specific formulations of

* Corresponding author.
E-mail address: lucia.ferrari9@unibo.it (L. Ferrari).

https://doi.org/10.1016/j.cemconcomp.2025.106452
Received 27 October 2025; Received in revised form 6 December 2025; Accepted 16 December 2025
Available online 19 December 2025

superplasticizers [24–27]. This effect is commonly attributed to the increased specific surface area (SSA) of LC3 particles [28,29], which reduces the amount of free water available for flow due to internal porosity [30,31].

From this perspective, rheology plays a key role in determining a material's extrudability and buildability, especially in the context of digital construction. In particular, 3D printing enables the use of construction materials in applications such as urban furniture with innovative designs, although this requires careful adjustment of their rheological and mechanical properties. As highlighted in the literature, yield stress, viscosity, and structuration rate are key parameters for printable concrete, as they govern whether a material can be extruded continuously and retain its shape after deposition [32,33]. Other studies explored developement of proper printed material's geometry and structure [34–36], structural failure during extrusion [35] and highlighted the need to assess the yield stress beyond the range commonly considered for fresh concrete [36]. Indeed, whereas the rheological properties of concrete are often studied in the range of several Pa, like for self-compacting concretes, they may reach the order of several tens to thousands of kPa in a 3D printing process. In this context, the accurate characterization of fresh-state properties in cementitious materials requires not only the use of new advanced rheological measurement systems but also ongoing innovation in the development of novel tests.

Complementary to experiments, numerical simulations provide powerful predictive tools for evaluating and optimizing printability by simultaneously accounting for the effects of material properties and printing parameters on both the process and the outcome. As a matter of fact, numerical simulations can replace costly and time-consuming trial-and-error campaigns for mix development and calibration. In the case of new materials, as in this study, they become essential for assessing feasibility from the outset, allowing researchers to proceed efficiently while minimizing material consumption. Over the past decade, different numerical models for 3D printing with cement-based materials have been developed. Solid single-phase Finite Element Method (FEM) models are among the most widely used; they typically reproduce the layer-by-layer deposition process by sequentially activating layers [37] or elements [38], predicting the occurrence of plastic collapse or elastic buckling and thereby assessing buildability. More recently, continuum fluid models and meshless methods have also seen increasing adoption, offering a more detailed representation of pumping, extrusion, and layer deposition, though generally at higher computational cost. For instance, CFD-based simulations have been performed in Ref. [39] using the Finite Volume Method (FVM) in FLOW-3D, and in Ref. [40] using the Particle Finite Element Method (PFEM), accurately predicting filament shapes in rectilinear layers and validating the results against experimental data. Such models can also be applied to investigate the influence of material and process parameters on filament geometry and morphology, enabling the identification of potential defects such as buckling or tearing [41,42].

This work fills the research gap on the rheology of LC3 mortars with recycled ceramics and introduces a novel approach that combines improved fresh-state testing with numerical simulations for additive manufacturing. Surface area and pore volume of dry powders was measured by N_2 sorption. The rheological behaviour of LC3-based mortars formulated with calcined clay (reference) and six different recycled ceramic powders in substitution of the clay was investigated. Fresh-state properties were assessed through flow table tests and rheometric measurements. The traditional slump test, commonly used to evaluate the workability of cementitious materials, is not well suited for low-slump mixtures, such as 3D-printable concretes, because it cannot accurately capture their fresh-state behaviour. Therefore, the flow table test has been proposed as a more appropriate method by Refs. [43,44]. Different rheological models were applied to estimate the yield stress and the thixotropy parameters. A specific sequence designed for a ball measuring system was developed as a test method suitable for evaluating static yield stress not only in the kPa range but also in highly viscous mixtures containing fine aggregates—relevant for 3D printing applications. The measured yield stress and viscosity were used to simulate the virtual printing process of all formulated mortars through the PFEM-based computational framework presented in Refs. [40,41]. Extrudability and filament quality were evaluated under two distinct device configurations, using a "WASP 40100 LDM" with a manual feeding system. This is the first in-depth study on the rheology of LC3-based mortars with recycled ceramics for additive manufacturing applications, highlighting a viable route to enhance sustainability while maintaining printability and performance.

2. Investigation rationale and programme

2.1. Materials

As part of this study, six companies from different sectors of the ceramic and construction industries located in the North-East of Italy were contacted to supply waste materials, generally labelled as Ceramic Waste (CW). Three of them operate in the manufacturing of ceramic materials: one provided waste powder from dry tile rectification (CW1); another provided large roof tile scraps (5–10 cm) (CW2); and the third one, a machinery manufacturer for the ceramic industry, supplied fired ceramic powders generated during machine testing (CW3). Additionally, a demolition waste management company provided finely ground ceramic waste, in the 0–4 mm range (CW4). Two companies specialized in grinding unsold ceramic tiles delivered fine ceramic aggregates (0–4 mm) (CW5 and CW6).

The materials supplied as scrap and core particles up to 4 mm were micronized in a rotary mill (Nonantola, Italy). A 300 g sample was ground for 20 min in ~1 L jars containing 20 ceramic spheres, each 20 mm in diameter. The resulting powder was sieved to obtain particles smaller than 300 μm, intended for use as partial cement replacement [45].

These ceramic powders were then combined with Ordinary Portland Cement (CEM I 52.5 R) and commercial limestone (LS), both provided by Heidelberg Materials, Germany. One calcined clay (CC) was also used as reference materials. The kaolinite content of the material before calcination was 41 %, and calcination was performed using the flash method at 800 °C [30]. The mineralogical composition of PC, limestone and calcined clay is reported in the supplementary materials (Supplementary Table 1) while the mineralogical characterization of ceramic waste is reported in Ref. [46].

The physical and chemical characterization of the powders included measurements of particle density, particle size distribution (PSD) and oxide composition by Inductively Coupled Plasma Optical Emission Spectrometer (Avio 550 Max ICP-OES, PerkinElmer, Italy). The PSD was measured in water for calcined clays, limestone and ceramic waste by a Malvern Hydro 2000MU, while CEM I was analysed by Malvern Mastersizer 3000 in isopropanol, due to their reactivity with water. Density was determined following EN 197-6 using the pycnometer method [47]. Materials' density and chemical composition are displayed in Table 1, while the PSD is reported in Fig. 1.

The mortar containing calcined clay or ceramic waste was prepared according to the following formulation: 237 g of CEM I, 71 g of LS, 142 g of calcined clay or ceramic waste, 225 g of deionised water and 1350 g of crushed natural sand, supplied by Italcementi (Bergamo, Italy), with particles diameter of 0–2 mm. No additional gypsum was introduced because the sulfate already contained in the CEM I was sufficient for the system, and previous tests confirmed that the calcined clay ensured adequate early-age reactivity, yielding 33 MPa of compressive strength of LC3 at 2 days [31]. The mixing was performed in a Hobart mixer according to EN 196–1:2016 [48]. A polycarboxylate ether-based superplasticizers (labelled as SP), with a 22 % solid content, was provided by CHRYSO SAINT-GOBAIN R&D laboratory in Sermaises (France). The SP was added to the measured amount of water at the specified dosage prior to mixing. The reactivity index of calcined clay

Table 1
Density and chemical composition of powder materials. LOI = Loss on Ignition.

Material	Density	Compound										
	(g/cm^3)	SiO_2	Al_2O_3	Fe_2O3	CaO	MgO	K_2O	Na_2O	SO_3	Others	LOI	Total
CEM I	3.08	19.2	5.1	3.2	62.7	1.9	1.0	0.1	3.3	0.5	2.5	99.5
LS	2.72	0.6	0.0	0.0	55.6	0.0	0.0	0.0	0.0	0.0	43.8	100.0
CC	2.70	60.2	25.8	8.9	1.0	0.2	0.2	0.0	0.1	1.3	2.4	100.0
CW1	2.61	72.1	22.8	1.0	0.8	0.2	1.1	0.6	0.0	0.9	0.4	99.9
CW2	2.75	66.1	18.6	6.1	3.1	1.8	1.5	0.2	0.5	1.0	1.1	99.9
CW3	2.65	65.5	20.5	2.1	3.4	1.5	2.4	2.9	0.2	1.5	0.0	100.0
CW4	2.82	45.3	7.0	2.3	18.5	1.5	2.1	1.2	1.1	0.3	18.6	97.9
CW5	2.53	68.1	21.2	0.9	1.3	0.4	2.8	3.7	0.1	0.8	0.7	100.0
CW6	2.50	68.3	20.3	1.1	1.9	0.4	3.1	3.6	0.2	0.8	0.4	100.0

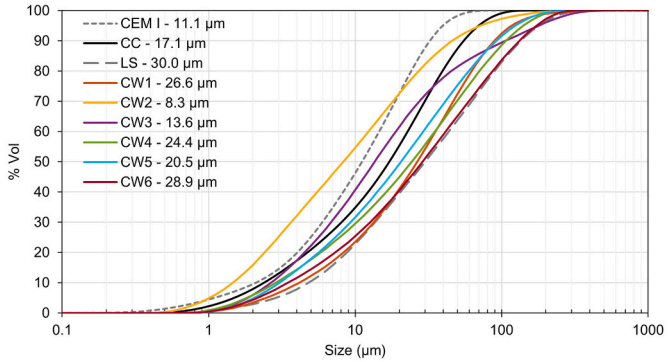

Fig. 1. PSD of the analysed materials. The diameters in the legend indicate the median particle size (d_{50}).

and ceramic waste and mechanical strenght of LC3 binders at 28 days are reported in Supplementary Table 2.

2.2. Methods

2.2.1. N_2 sorption

SSA is increasingly recognized as a key property of modern SCMs, in particular for calcined clay where SSA directly affects their reactivity, the water demand, and the overall performance in cementitious systems. In this study, a detailed assessment of SSA was carried out, together with specific pore volume (SPV) by Brunauer–Emmett–Teller (BET) method, which emerged as a critical parameter influencing the rheological behaviour of fresh mixtures [30].

SSA and SPV were measured using nitrogen adsorption with a Nova 800 BET Analyzer (Anton Paar Italia S. r.l.). Samples (0.2–0.6 g) were first degassed for 15 min at 150 °C to remove moisture, then analysed via nitrogen adsorption isotherms. The specific surface area and cumulative pore volume were derived from N_2 adsorption isotherms of mesoporous and microporous powders using density functional theory (DFT), applying a DFT-based Kaomi model implemented in the Nova PC software [49], an approach widely used to quantify pore size distributions in both conventional and novel nanoporous solids. This combined approach enabled a precise evaluation of both surface and pore characteristics, explaining the impact of internal porosity on yield stress and workability in waste-based binders.

2.2.2. Flow table test

The flow table test aimed to find the SP dosage for the reference mix in order to provide a similar consistency of all mortars. Measurements were performed according to ASTM C1437 − 20 standard [50] on fresh mortar samples 10 min after mixing. A truncated cone (60 mm height, 100 mm bottom diameter, 70 mm top diameter) is filled with the mixture, compacted, and subjected to jolting on a flow table. The average spread diameter was recorded after 5, 10, 15, 20, and 25 drops.

The model by Kurokawa [51] was applied to estimate the yield stress of the mortars, using the following equation:

$$\tau_n = \left(\frac{\rho g V}{25\sqrt{3}\pi {D_n}^2}\right)\cdot 10^8 \quad \text{(Eq. 1)}$$

where τ_n (Pa) is the estimated yield stress after n drops, ρ (kg m^{-3}) is the density for each different mix, g (9.81 m s^{-2}) is the gravitational acceleration, V (0.000344 m^3) is the total volume of the cone used in the test, D_n (mm) is the average diameter measured every 5 shakes. The Kurokawa equation has been shown to better fit flow-table data for stiff, 3D-printable mortars [52], whereas other models [53] are more appropriate for highly fluid mixtures and do not adequately represent the rheology of the materials investigated in this study. To determine the initial static yield strength of each mix, a second-degree polynomial curve was applied as proposed by Ref. [52].

2.2.3. Rheological measurements

The rheological characterization of the mortars was performed using an Anton Paar MCR 302 rheometer equipped with the Ball Measuring System (BMS) [54], to determine the static yield stresses. The static yield stress is the shear stress at which a solid-like material begins to flow, marking the onset of deformation. In contrast, the dynamic yield stress represents the minimum shear stress required to sustain flow. Below the dynamic yield stress, the material reverts from a fluid-like to a solid-like state. The BMS consists of a rotor and a cylindrical cup with an inner diameter of about 115 mm, accommodating roughly 500 mL of sample. The rotor is made of a radial arm mounted perpendicularly to the shaft, which holds a downward-pointing pin ending with a spherical ball of diameter 8 mm (see Fig. 2). When the rotor operates, the ball moves through the sample along a circular path.

At 10 min, a flow curve test protocol was performed with a logarithmic ramp of decreasing share rate from 100 to 0.1 s^{-1}. This served to homogenise the material in the cell and extract the initial viscosity. Since the ball penetrates unsheared material only during the first rotation, a specific measurement sequence was designed with the rheometer's software RheoCompass to determine the static yield stress at different hydration time. After the viscosity curve, a stress growth

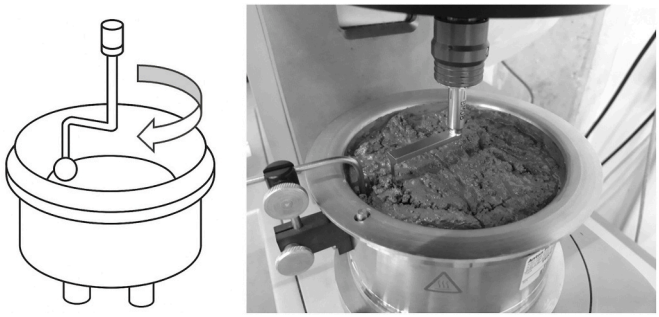

Fig. 2. Illustrative diagram (left) and pictures (right) of the BMS.

protocol with stress imposed was applied, as proposed by Ref. [55]. This method, in opposition to stress development under constant shear rate, is independent on the applied shear rate and is particularly effective to determine the static yield stress [56]. The first quarter of the sphere-rotation was used for the shear stress ramp at 15 min, the second quarter for 30 min, the third quarter for 45 min, and the final quarter for 60 min, as illustrated in Fig. 3. A resting period occurred between measurements, during which the sample was left in the cell.

In each shear stress ramp, the applied shear stress was increased following a logarithmic ramp from 10 to 5000 Pa, and the measurement was stopped before reaching a deflection angle of 500 mrad corresponding to a shear strain of about 100–150 %. Repeated measurements were performed at 15, 30, 45 and 60 min. The static yield stress was determined from flow curves obtained through the shear tress ramp. In these curves, the yield point is defined as the highest shear stress at which the rheometer still detects no movement (corresponding to a deflection angle below 500 mrad), as proposed by Ref. [55]. If the rheometer detects the first non-zero velocity, the yield point has already been exceeded, and the motion of the sphere is stopped to prevent disruption of the resting mortar (see Fig. 4).

Thixotropy was also accounted for by including the time-dependency of the static yield stress parameter according to Roussel's model [57]:

$$\tau_0(t) = \tau_{0,i} + A_{thix}t \qquad \text{Eq. 3}$$

where $\tau_{0,i}$ is the initial static yield stress, A_{thix} is the structuration rate and t is the material hydration time. It should be noted that the time was always measured from the first contact between the water and the binder, whereas the effective resting period of the sample starts 15 min later. Therefore, this 15-min point can be considered as the true t = 0 for the resting time.

2.2.4. Numerical simulation

Numerical simulations provide a fast and cost-effective means to preliminarily assess the extrudability and buildability of newly developed mixes. In this work, tAs an input to the simulations, the rheological experimental data were analysed assuming a purely viscoplastic material behaviour, according to the Bingham constitutive model:

$$\begin{cases} \tau(u) = 2\mu\epsilon(u) + \tau_0\dfrac{\epsilon(u)}{\|\epsilon(u)\|} & if\ \|\tau\| > \tau_0 \\ \epsilon(u) = 0 & otherwise \end{cases} \qquad \text{Eq. 2}$$

where $\boldsymbol{u}$ represents the velocity, $\boldsymbol{\tau}(\boldsymbol{u})$ is the deviatoric stress tensor, μ is the Newtonian viscosity, τ_0 is the yield stress and $\boldsymbol{\epsilon}(\boldsymbol{u})$ is the deviatoric strain rate tensor. The 3D printing computational framework introduced in Ref. [40], based on the Particle Finite Element Method (PFEM) [58], a robust numerical approach for simulating multi-physics problems in evolving domains, is adopted. PFEM solves the Navier–Stokes equations for continuum fluids within an updated Lagrangian formulation. Mesh distortion is avoided by remeshing once excessive deformation occurs, using a combination of Delaunay triangulation and the alpha-shape method [59].

Key features have been incorporated into the PFEM framework to capture extrusion and layer deposition in 3D printing [40]. These include tailored algorithms for enforcing complex boundary conditions (e.g., inlet flow and interlayer contact), as well as strategies to improve efficiency through adaptive de-refinement and CPU parallelization. The model is implemented in an in-house FEM code developed at Politecnico di Milano and validated against experimental data for both single- and multi-layer walls. Further validation was presented in Ref. [41], where the model was benchmarked against results from independent research groups using different cement-based materials, and a parametric study was conducted to assess the influence of material and process parameters on filament morphology. The framework is also under extension to include more complex material behaviors, such as thixotropy [60] and elasticity effects [61,62].

Finally, it is worth mentioning that, due to the difficulties in capturing the sharp phase transition, in the numerical model it was preferred to implement the Papanastasiou regularization of the Bingham law [63].

2.2.5. 3D printing framework

A WASP 40100 LDM 3D printer was selected for both the numerical simulations and the subsequent experimental validation; therefore, the printing parameters were chosen to remain fully compatible with the operating capabilities of this machine. Two representative sets of parameters were defined as reported in Table 2. The first set, suitable for medium-scale objects, employed a 10 mm nozzle diameter, a 7 mm nozzle height, a material flow velocity of 80 mm/s, and a printing speed of 60 mm/s. These velocities fall within the typical ranges identified in Ref. [42] as representative of practical medium to large-scale extrusion processes. In addition, by selecting a flow velocity slightly higher than the printing speed and a nozzle height smaller than the nozzle diameter, a layer-pressing strategy is obtained [41,64]. Layer-pressing is widely adopted in practice because it promotes flatter deposited layers, reduces geometric uncertainty, and improves interlayer bonding. The second set was designed for smaller objects, where higher precision and finer geometric features are required. A smaller nozzle diameter (7 mm)

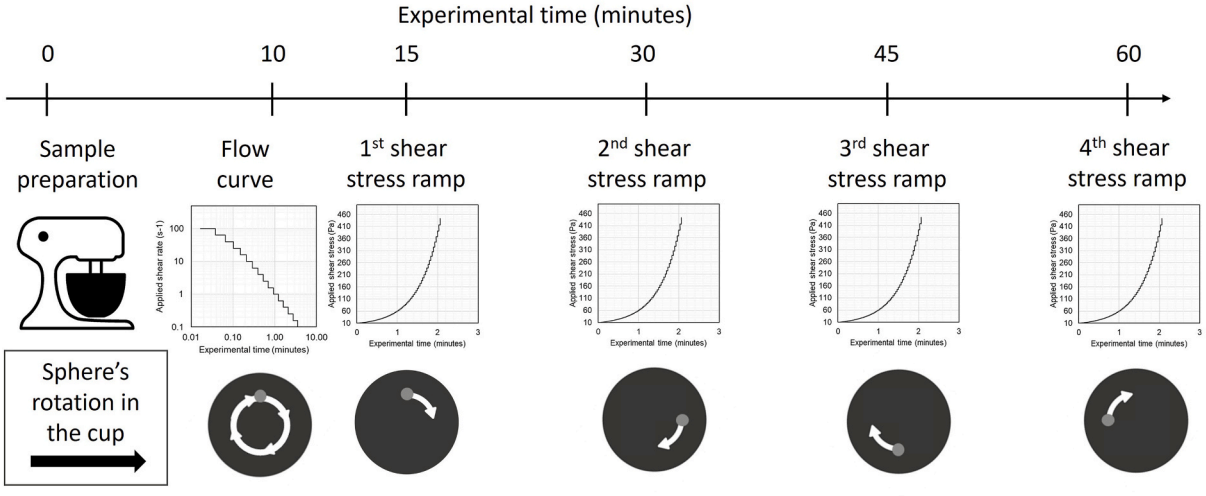

Fig. 3. Schematic representation of the sequence designed with rheometer's software RheoCompass to measure viscosity and static yield stress as function of time.

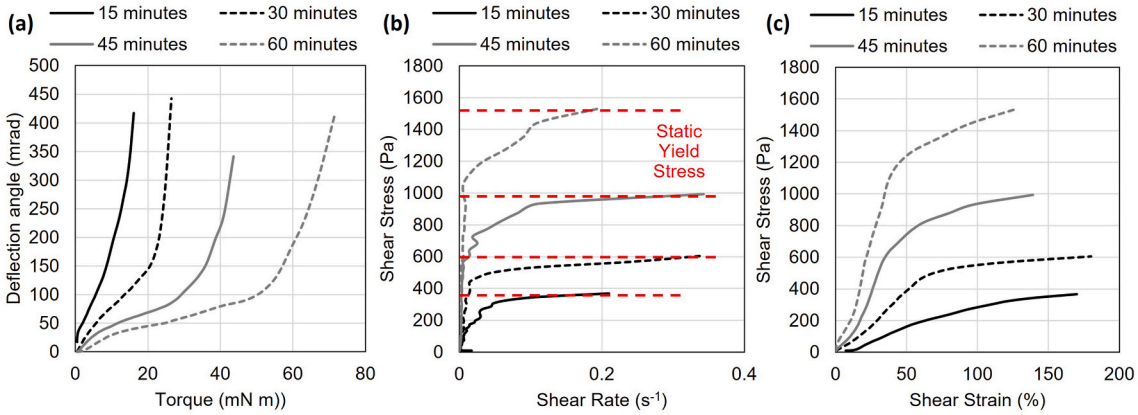

Fig. 4. Illustrative scheme of the rheological measurements: deflection angle as a function of the applied torque (a); flow curve with the estimation of the static yield stress determined as the point at which the shear rate becomes different from zero (b); representation of the shear stress-shear strain plot (c).

Table 2
Printing settings used in the extrudability numerical study.

	Nozzle diameter (mm)	Nozzle height (mm)	Flow velocity (mm/s)	Printing speed (mm/s)	Wall length (cm)
1st framework	10	7	80	60	50
2nd framework	7	5	5	5	10

combined with a reduced nozzle height (5 mm) still ensures a mild layer-pressing effect. The reduced dimensions, together with lower flow velocity (5 mm/s) and printing speed (5 mm/s), provide better control of the deposited filament and enable a narrower filament width.

To validate the numerical simulation, preliminary 3D printing tests were performed using the aforesaid WASP 40100 LDM printer (Wasp, Italy) equipped with a manual extruder. Three mixes were selected, namely LC3-CC, LC3-CW1, and LC3-CW3, and a few layers of material were deposited. The printer was operated with a 7 mm nozzle and a layer height of 5 mm. To ensure homogeneous feeding, the sand was sieved at 1 mm to remove coarse particles, and only 300 g were incorporated into the cement paste. This adjustment was necessary because the mixing screw inside the funnel was unable to generate enough shear and pressure to ensure continuous extrusion of the mortar filament. The modification was applied to all printed mixtures to maintain comparability. Despite the difference in aggregate size between rheological tests and printing, the comparison between binders and different ceramic sources remains valid, as this comparative evaluation allows assessing their relative extrudability and buildability. Although the simulations were conducted on straight filaments, the experimental validation was carried out by printing circular paths, which reduced the effects of layer instability and stresses induced by the printer, and enabled continuous material extrusion, which was particularly critical in the used mixes. The printing process and the printed objects were qualitatively assessed with respect to deformation, including shape retention, edge stability, and interlayer adhesion. This analysis is intended as a preliminary proof of concept, aimed at comparing the behaviour of the different mixes, supported by the quantitative assessment provided by the numerical simulations, for an overall validation of the proposed approach.

3. Results

3.1. Powders properties

N_2 adsorption and desorption isotherm isotherms of raw materials and calcined clays are displayed in Fig. 5 and in Table 3. The results highlight the large differences in microstructural properties among the investigated raw materials. CEM I and LS exhibit negligible adsorption, in agreement with their very low SSA (0.06 and 0.60 $m^2\ g^{-1}$, respectively) and SPV below 0.01 $cm^3\ g^{-1}$. In contrast, CC displays a much higher surface area (48 $m^2\ g^{-1}$) and pore volume (0.108 $cm^3\ g^{-1}$), reflecting the maintenance of interlayer voids during dehydroxylation of the clay minerals. The ceramic wastes (CW1–CW6) show intermediate adsorption capacities, with SSA values ranging from 0.76 to 4.12 $m^2\ g^{-1}$ and pore volumes between 0.002 and 0.018 $cm^3\ g^{-1}$. However, the notably higher SPV and SSV values for CW4 are attributed to its origin from construction and demolition waste, which contains highly porous brick fragments and residual cement paste. These values are significantly lower than those of CC, showing that the thermal history of the ceramic materials has already led to partial sintering and reduction of accessible surface area. The isotherms mainly correspond to type IV with H3-type hysteresis, typically associated with mesoporous solids containing slit-shaped pores formed by plate-like particles, although the nearly flat profiles of LS and CEM I resemble type II, consistent with nonporous or macroporous solids [65]. Notably, the SPV has been shown to be a critical parameter controlling the rheological properties of suspensions, as higher pore volumes promote stronger water adsorption and consequently higher water demand [30]. Therefore, the rheological behaviour of pastes containing CC is expected to be markedly different from that of mixes incorporating CW, where the limited pore volume suggests a much weaker impact on water uptake and flowability.

3.2. Rheological properties by flow table test and ball measuring system

The estimated yield stress and spread vs. drops obtained at the flow table tests are displayed in Fig. 6. For LC3-CWs mixtures, 0.1 % SP produced an estimated yield stress of ~450 Pa, which we used as the target reference value. To achieve a comparable rheological response in LC3-CC, a much higher SP dosage was required, and 0.4 % was identified as the dosage needed to reach a similar yield stress (424 Pa). Therefore, 0.4 % was selected as the appropriate dosage for LC3-CC. At these dosages, the rheological behaviour of LC3-CC is not more critical than that of the CW systems; the main distinction, however, is its substantially higher SP demand. This behaviour can be directly linked to the microstrctural properties of the powder: the markedly higher SPV of CC (0.11 $cm^3\ g^{-1}$) compared to CW materials (<0.02 $cm^3\ g^{-1}$) leads to stronger water absorption within the internal particles porosity, reducing the free water available for fludifcation and necessitating

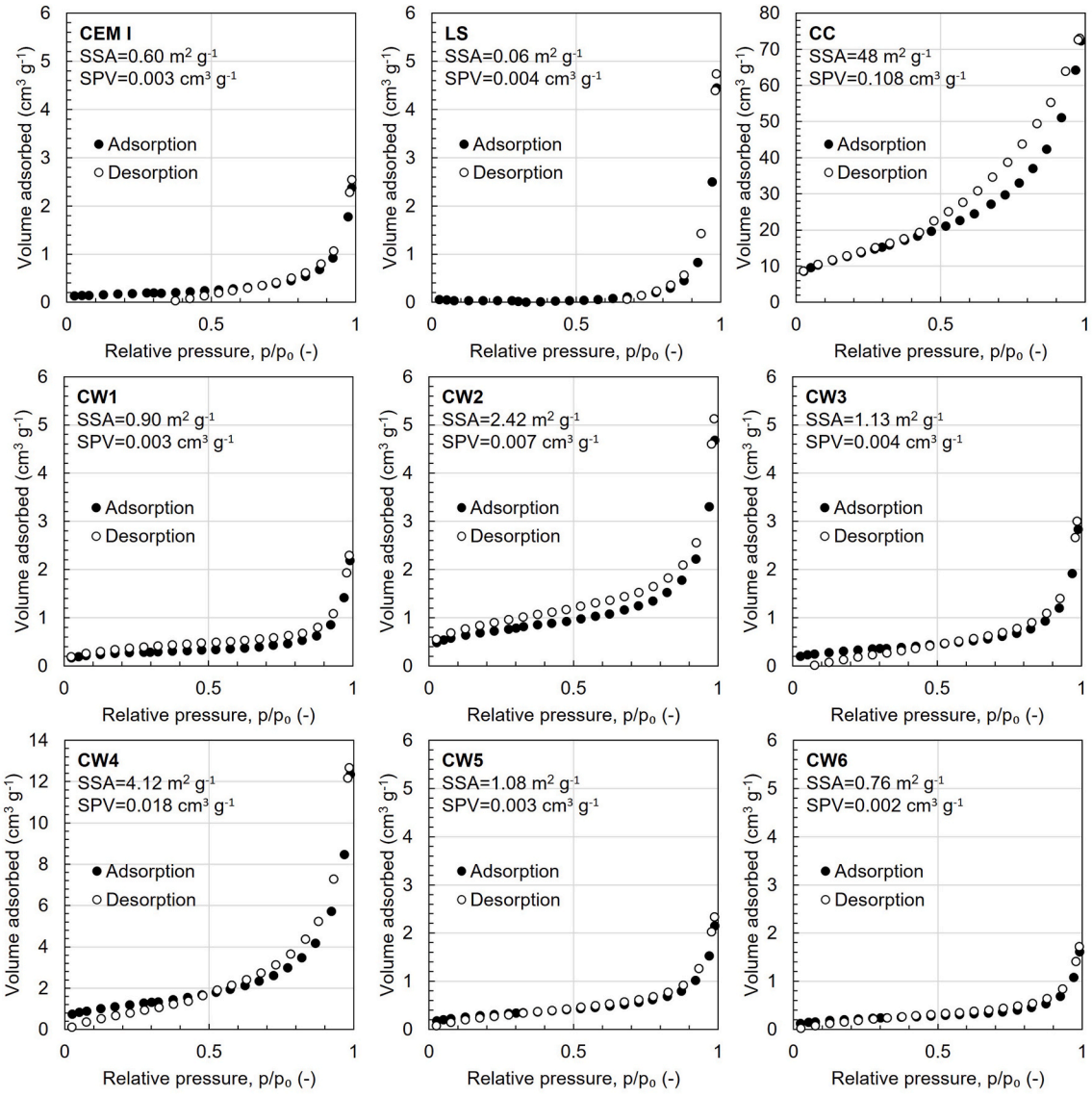

Fig. 5. N_2 adsorption and desorption isotherms of the dry powders. Calculated values of SSA and SPV are reported in the plot area. For better visibility of data, CC and CW4 are plotted with a different scale.

Table 3
Resume of SSA and SPV for each material.

Sample	CEM I	LS	CC	CW1	CW2	CW3	CW4	CW5	CW6
SSA (m^2/g)	0.60	0.06	48	0.90	2.42	1.13	4.12	1.08	0.76
SPV (cm^3/g)	0.003	0.004	0.108	0.003	0.007	0.004	0.018	0.003	0.002

greater SP addition to reach a comparable initial workability. The evolution of yield stress and spread diameter with drop number in all systems is well described by a second-degree polynomial fit, in agreement with the approach proposed in Ref. [52].

The shear stress versus shear strain behaviour of mortar samples incorporating calcined clay (LC3-CC) and various ceramic waste materials (LC3-CW1 to LC3-CW6), evaluated at rest intervals of 15, 30, 45, and 60 min is illustrated in Fig. 7. The viscosity and the extracted static yield stress values, determined as the highest stress at which no motion occurs, are reported as well in the same figure. It is important to note that viscosity is determined at higher shear rates and therefore characterises flow behaviour under deformation, whereas static yield stress reflects the material response at rest and is less influenced by viscosity. The latter is evaluated only after sufficient angular deformation is reached under increasing torque (see Fig. 4), and is unaffected by shear rate since stress, not rate, is imposed.

All samples exhibit non-linear stress–strain relationships and typical thixotropic behaviour with all mixtures showing a progressive increase in static yield stress as the resting period increases. Notably, LC3-CC and LC3-CW3 display the highest shear stress values at extended rest times (45 and 60 min), indicating pronounced structural buildup. In contrast, LC3-CW2 and LC3-CW5 show the lowest thixotropic response, suggesting a weaker internal network formation over time. The increased dosage of superplasticizer (SP) lowers the initial static yield stress of LC3-CC; however, it does not fully offset the workability reduction commonly associated with this type of material. Differences among the CW systems suggest that the specific composition strongly influences the structuration rate and final yield stress, with some formulations showing

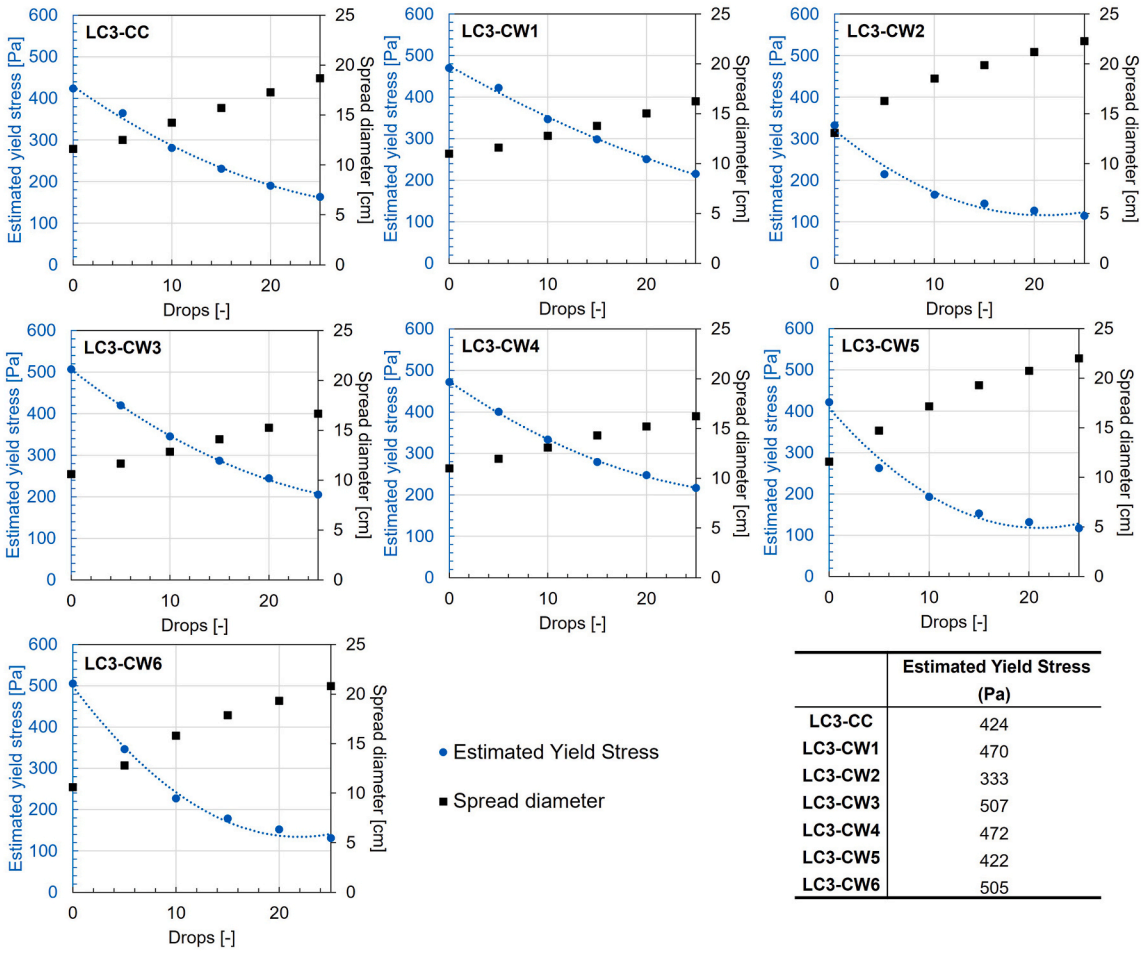

	Estimated Yield Stress (Pa)
LC3-CC	424
LC3-CW1	470
LC3-CW2	333
LC3-CW3	507
LC3-CW4	472
LC3-CW5	422
LC3-CW6	505

Fig. 6. Spread diameter and estimated yield stress obtained with the flow table test. The fitting is obtaiend with a polynomial curve of degree 2 as suggested in [52].

faster build-up already at 15 min (e.g., LC3-CW6), while others remain comparatively less sensitive at early ages (e.g., LC3-CC and LC3-CW2).

It is worth noting that minor artifacts may arise in rheological measurements due to the presence of coarse aggregate particles (maximum size of 2 mm) positioned directly in the trajectory of the rotating sphere within the rheometer cell. Such localized obstructions can momentarily distort the stress–strain curve. However, no major anomalies or defects are detectable in the presented data, and the overall trends remain consistent and interpretable across all samples.

Fig. 8 presents the time-dependent evolution of static yield stress. Each plot displays a linear regression fit, with slope values representing the rate of structural buildup over time interpolated according to Eq. (3) in order to extrapolate the A_{thix} value. Although R^2 values are not explicitly shown, all fittings resulted into $R^2 > 0.94$, confirming the high consistency of the applied model. Since the resting time only begins at 15 min, the intercept of the linear regression at 0 min is not relevant. A more meaningful reference would be the value predicted by the regression at 15 min. LC3-CC, LC3-CW3 and LC3-CW6 exhibit the steepest slopes, with values of A_{thix} corresponding to nearly 102, 79 and 84 Pa/min respectively, indicating the most pronounced thixotropic behaviour and rapid structuration. In contrast, LC3-CW2 and LC3-CW5 show the lowest slopes, with values of A_{thix} corresponding to 36 and 28 Pa/min, reflecting minimal structural buildup and weaker thixotropic response. LC3-CW1 and LC3-CW4 show an intermediate behaviour. In most cases, the substitution of calcined clay with ceramic waste leads to a broadly consistent reduction in static yield stress across all CW samples, resulting in improved fluidity and workability—beneficial for applications such as pumping, casting, and minimizing formwork pressure.

The rheological behaviour can be analysed in respect to the SSA, which strongly influences mortar rheology by controlling water demand and the availability of free water [30,31]. If the available free water is reduced, the interparticle distance automatically increases generating stronger interparticle attractive forces and higher effective solid volume fraction [66]. These factors partially explain the observed differences in static yield stress and structuration rate among the studied systems, with higher SSA generally leading to faster and stronger build-up. From a practical perspective, this highlights the need to tailor water-to-binder ratio and admixture dosage to the SSA of the material in order to achieve consistent workability and stability. In the proposed analysis, the significantly higher SSA provided by CC drastically increased the SP demand required to achieve comparable workability to other mixes containing CW, which have much lower SSA and, in particular, lower SPV. However, SSA alone cannot fully explain the results. The chemistry of the materials also plays a critical role, as it governs their intrinsic reactivity. In particular, the potential differences in the formation of ettringite can alter particle interactions and lead to an evolution of SSA with time [63], thereby further impacting the rheological response [67,68]. The Al_2O_3 content was around 20 % for all CWs and CC, suggesting a similar potential for ettringite formation. However, CW4, which exhibited the lowest Al_2O_3 content, also displayed a much higher CaO content (18.5 %, compared to below 3.5 % in the other CWs). This elevated CaO likely accelerates early hydration and structuration, contributing to the higher yield stress and faster stiffening observed in CW4. Both physical (SSA-related) and chemical (reactivity-driven) contributions must therefore be considered to fully understand and predict the rheology of these systems.

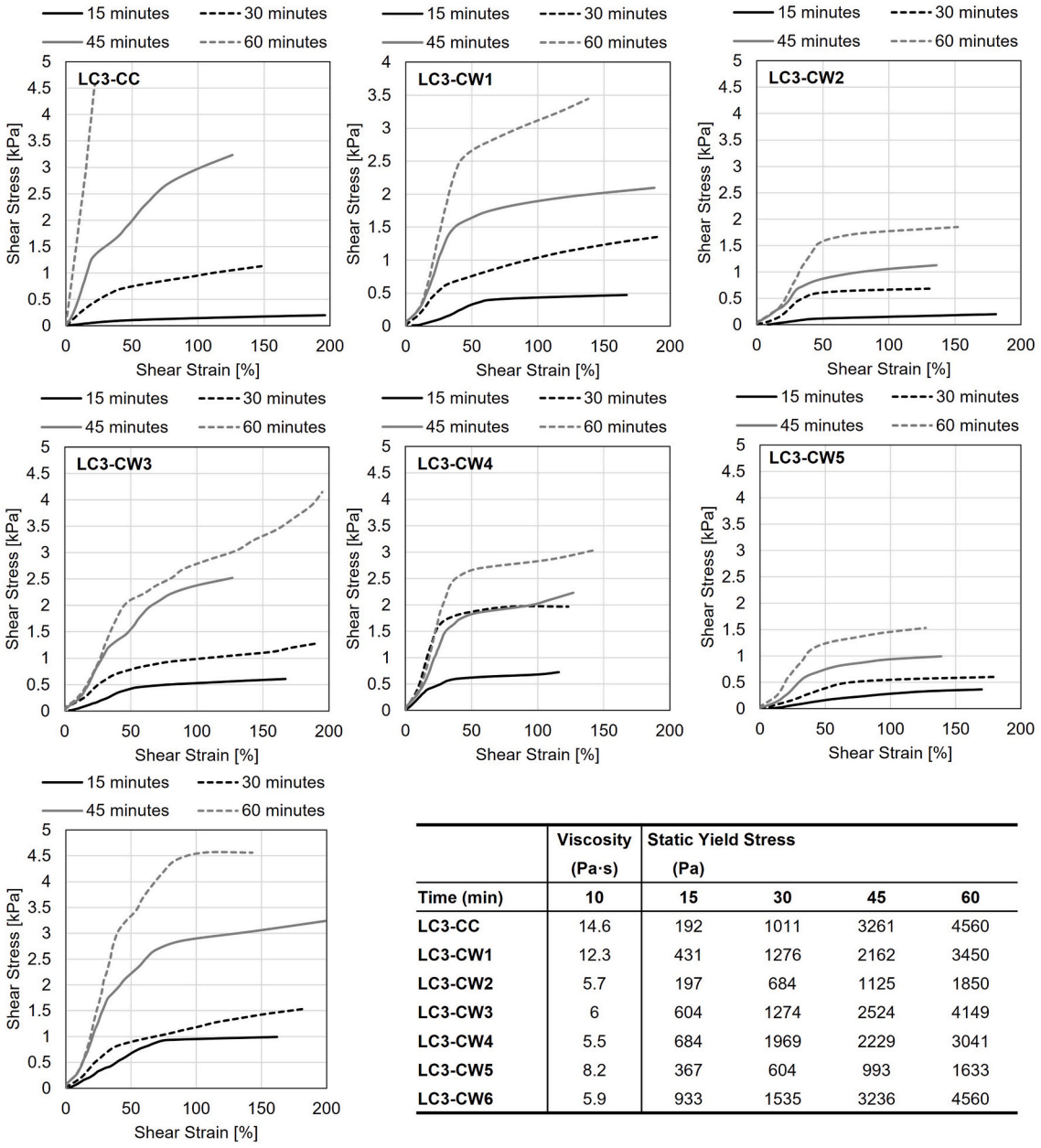

	Viscosity (Pa·s)	Static Yield Stress (Pa)			
Time (min)	**10**	**15**	**30**	**45**	**60**
LC3-CC	14.6	192	1011	3261	4560
LC3-CW1	12.3	431	1276	2162	3450
LC3-CW2	5.7	197	684	1125	1850
LC3-CW3	6	604	1274	2524	4149
LC3-CW4	5.5	684	1969	2229	3041
LC3-CW5	8.2	367	604	993	1633
LC3-CW6	5.9	933	1535	3236	4560

Fig. 7. Stress-strain curves obtained with rheological measurements on mortar at different hydration time and table estimatred viscosity and static yield stress.

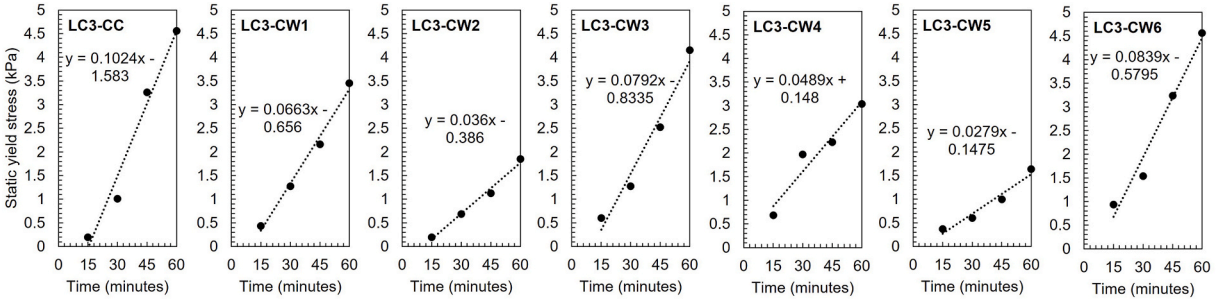

Fig. 8. The static yield stress as function of time. The linear fit represent the estimation of the structuration rate A_{thix}.

For the first time, the BMS was used to directly quantify the static yield stress of cementitious pastes and mortars, offering high sensitivity to structuration and thixotropy. It provides fundamental rheological parameters essential for constitutive modelling and simulations of processes such as 3D printing, pumping, and casting, where classical rheometers often fail due to the very high yield stress of mortars (kPa) and

their limited applicability to pastes. In contrast, the **flow table test** gives an indirect, empirical measure of workability, mainly reflecting yield stress, viscosity, and thixotropy under large deformations, but is less sensitive to early structuration. Both methods are thus valid and complementary to assess the fresh-state consistency in 3D-printed mortars: the BMS offers detailed, research-grade insights, while the flow table provides a practical field-oriented evaluation.

3.3. Assessment of the extrudability and buildability via numerical simulation

The printing of rectilinear walls, each consisting of five superimposed layers, was simulated using the PFEM numerical framework introduced before. A total of 14 simulations were conducted to assess the influence of the two printing frameworks defined in Table 2 on the seven developed LC3 mixes. The material properties employed for each mix are those derived from rheometric tests and are summarized in Table 4.

Fig. 9 presents qualitative 3D views of the virtually printed geometries. The first row corresponds to the printing of rectilinear walls with a length of 50 cm, simulated using the first parameter set in Table 3, with a 10 mm diameter nozzle. All mixes appear extrudable, but some of them (e.g., LC3-CC and LC3-CW2) exhibit pronounced plastic deformations in the bottom layers, whereas the other mixes appear more buildable, showing varying degrees of vertical deformation, primarily visible at the edges. The second row refers to the printing of 10 cm-long rectilinear walls using the second parameter set reported in Table 2, associated to 7 mm diameter nozzle. Under these conditions, all mixes appear both extrudable and buildable, demonstrating that the choice of printing parameters strongly influences the suitability of materials for printing. Proper selection of nozzle size, layer height, and extrusion settings enables the successful fabrication of structures while controlling deformation, ultimately allowing different mixes to reveal their intrinsic buildability and stability characteristics.

Fig. 10 shows the wall cross-sections at the deposition of the fifth layer, extracted at midspan to minimize boundary effects. Fig. 10-a compares results with the first parameter set of Table 4: mixes LC3-CW3, LC3-CW4 and LC3-CW6 exhibit minimal deformation; LC3-CW1 and LC3-CW5 show intermediate deformation, while LC3-CC and LC3-CW2 undergo pronounced vertical deformation and squeezing of the bottom layers. These deformations can be attributed to insufficient yield stress in the lower layers, which makes them unable to sustain the cumulative weight of the upper layers. Improving the buildability of these mixes would require some adjustments in composition, such as modifying the water-to-binder ratio or superplasticizer dosage. Alternatively, altering the geometry or scale of the printed structure could help. For example, extending the printing time between successive layers would allow yield stress to increase more due to thixotropy and early-age hydration.

Table 4
Material properties of the developed mixes employed in the numerical study.

Label	Density (kg/m^3)	Viscosity (Pa·s)	Initial static yield stress (Pa)	Roussel thixotropy index (Pa/s)
LC3-CC	2236	14.6	192	1.71
LC3-CW1	2231	12.3	431	1.10
LC3-CW2	2239	5.7	197	0.60
LC3-CW3	2234	6.0	604	1.32
LC3-CW4	2242	4.5	684	0.81
LC3-CW5	2227	8.2	367	0.47
LC3-CW6	2226	5.9	933	1.40

Fig. 10-b presents the results obtained with the second parameter set (Table 4), characterized by a smaller nozzle. In this case, although mixes LC3-CC and LC3-CW2 still show greater deformations compared to the other mixes, overall deformations are considerably reduced, and all mixes can be regarded as buildable. This improvement results from the smaller nozzle diameter (7 mm), which produces lighter filaments requiring less yield stress to remain stable. Additionally, the lower printing velocity slows down the process, providing more time for the material to gain strength before the subsequent layer is deposited. However, this second printing setup is best suited for small-scale objects and decorative applications.

To provide a more quantitative evaluation of wall deformation and to better illustrate how variations in rheological properties influence the final printed geometry, Table 5 comparison between the total height and the spreading of the first (base) layer, measured at the end of the fifth printed layer, relative to an ideal reference geometry. The reference total height is defined as five times the nozzle height, while the reference width corresponds to that of the first layer in the wall exhibiting the least vertical deformation. This choice is justified by the assumption of material incompressibility in the numerical model, which implies that significant horizontal deformation cannot occur without a corresponding vertical deformation. Based on these definitions, the reference total height for printing framework 1 is 35 mm, while the reference first-layer width corresponds to that of mix LC3-CW6, equal to 18.6 mm. For printing framework 2, the reference height is 25 mm, and the reference first-layer width - again corresponding to mix LC3-CW6 - is 8.5 mm.

In Framework 1, LC3-CC showed the largest total height reduction (13.6 %), indicating lower structural stability during printing. Mixes incorporating ceramic wastes generally exhibited smaller height reductions, with LC3-CW3, LC3-CW4, and LC3-CW6 showing minimal reductions (2.8 %, 2.9 %, and 1.8 %, respectively), demonstrating better buildability. The first-layer width increased most for LC3-CC and LC3-CW2 (35.7 % and 32.5 %, respectively), reflecting higher flow, whereas LC3-CW3, LC3-CW4, and LC3-CW6 showed minimal width increase (3.6 %, 3.1 %, and 0.0 %), suggesting improved dimensional control and rheological stability.

In Framework 2, total height reductions were very small for all formulations ($\leq$2.1 %), confirming stability at smaller scales. First-layer width variations were also limited, with the highest increase observed for LC3-CW2 (12.8 %), while LC3-CW3 and LC3-CW6 remained nearly unchanged (0.1 % and 0.0 %), indicating consistent extrusion and deposition.

These simulations enable the prediction of material printability and provide a quantitative framework for selecting materials according to the printing setup and intended application. Materials with a low initial yield stress are unable to maintain the intended shape during deposition, making them more suitable for smaller nozzle diameters and smaller-scale objects. The results of these numerical simulations are particularly valuable in the context of industrial waste, where material variability is high and consistent printability is challenging to achieve.

In conclusion, the simulations provided reliable, case-specific predictions of material printability and offer a quantitative basis for selecting mixtures suited to specific printing setups and applications. Materials with low initial yield stress ($<$250 Pa) cannot retain their shape during deposition and are therefore better suited for small nozzle diameters or small-scale objects. Yield stresses between 250 and 900 Pa allow the formation of stable layers that withstand vertical loading, while larger nozzles ($>$3 cm) or taller printed elements ($>$5 layers) would demand higher yield stresses (1–10 kPa) to maintain structural integrity. Yet, mixtures above roughly 5 kPa become difficult or even impractical to pump and extrude. For this reason, materials with high thixotropy ($>$1 Pa/s) are promising for larger-scale printing, as their rapid structural build-up compensates for the need for higher static yield stress [69]. Viscosity, consistent with findings from Ref. [42], has only a limited effect on shape retention, though excessively high values can hinder pumping. The materials developed in this study fall within the

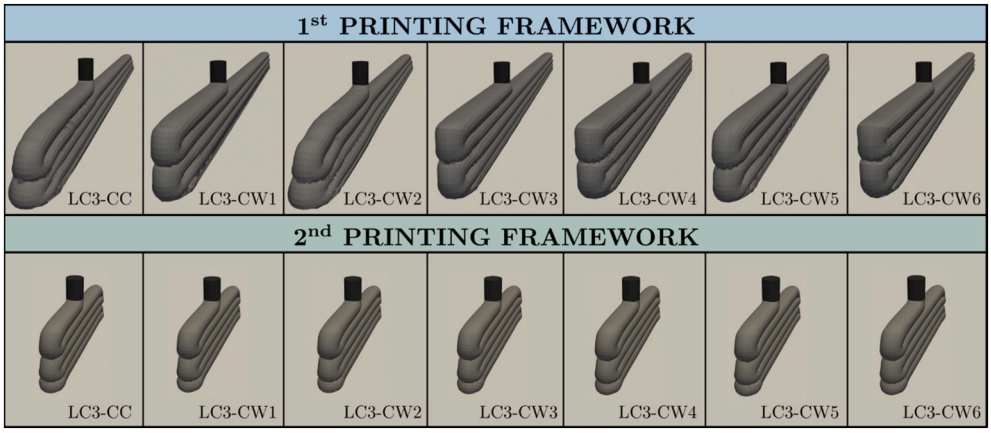

Fig. 9. 3D view of the virtually printed walls obtained with the two sets of printing parameters (note: the two sets are shown at different scales).

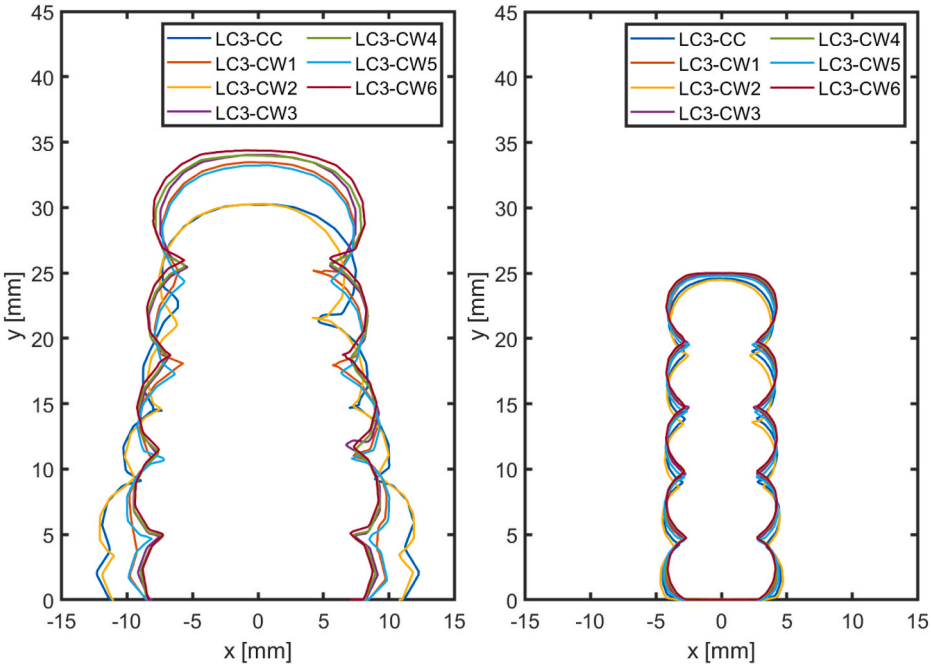

Fig. 10. Comparison of the cross-sectional shapes of filaments printed with the different materials under study, using nozzles of 10 mm (a) and 7 mm (b) diameter respectively.

workable range of 5–50 Pa s [41]-indeed all below 20 Pa s - ensuring smooth pumping and extrusion. Overall, these numerical results are particularly valuable when working with industrial waste materials, where variability is high and achieving consistent printability is often challenging.

4. Concept's validation with 3D printer

The preliminary experimental 3D printing trials are reported in Fig. 11 and demonstrated that the three investigated systems, LC3-CC, LC3-CW1, and LC3-CW3, exhibited a substantially similar printing response. Layer deformation is negligible, with high shape retention of the printed filament. Moreover, edges remained stable over time with sufficient interlayer adhesion. Although the simulation employs a linear path and the experiments use a circular path, the comparison is valid because the analysis of simulation focuses on the cross-section of the printed layer, which is independent of path geometry. Thanks to the optimized parameters adopted in this study, namely a 7 mm nozzle diameter and a 5 mm layer height, all mixes showed stable extrusion and consistent filament deposition, without marked differences in deformation or shape retention. It should be noted that, although LC3-CC and LC3-CW1 exhibit lower initial static yield stress compared to LC3-CW3, their viscosities (14.3 and 12.6 Pa s, respectively) are significantly higher than that of LC3-CW3 (6.0 Pa s). This fact facilitated easier extrusion for LC3-CW3 and resulted in slight layer spreading. Furthermore, the thixotropy index of LC3-CC is markedly higher than that of the mixes containing ceramic waste, promoting rapid structuration and improved stability over time. These aspects, however, do not appear to be dominant in the simulation, while they were qualtitavely observable in practice. Further experimental investigations are therefore required to provide a more quantitative explanation of the observed behaviour. These results contribute to confirm the crucial role of printing parameters in assessing material suitability for addtivi manifacturing, as the same mixtures could potentially show different behaviors under alternative conditions. This proof-of-concept demonstration successfully established the potential of ceramic waste materials for 3D printing applications. Rheological parameters extracted from rheological characterization were successfully used in simulations to predict the

Table 5
Comparison between the total height and the spreading of the first (base) layer.

	LC3-CC	LC3-CW1	LC3-CW2	LC3-CW3	LC3-CW4	LC3-CW5	LC3-CW6
FRAMEWORK 1							
Total height [mm]	30.2	33.5	30.3	34.0	34.0	33.2	34.4
Total height reduction [%]	13.6	4.4	13.5	2.8	2.9	5.0	1.8
Width 1st layer [mm]	24.6	19.6	24.0	18.8	18.7	20.0	18.1
Width increase 1st layer [%]	35.7	8.0	32.5	3.6	3.1	10.5	0.0
FRAMEWORK 2							
Total height [mm]	24.6	24.9	24.5	24.9	25.0	24.8	25.0
Total height reduction [%]	1.6	0.5	2.1	0.3	0.0	0.8	0.0
Width 1st layer [mm]	9.0	8.6	9.4	8.3	8.5	8.8	8.3
Width increase 1st layer [%]	8.1	3.3	12.8	0.1	2.0	5.7	0.0

printability of these materials. These simulations are therefore valid for two main purposes: identifying the appropriate printing setup and selecting the suitable material for the intended application, which is particularly important for waste-based materials with highly variable particle characteristics. Quantitatively, the simulations captured the relative stability of different mixes, providing guidance on nozzle size, layer deposition strategy, and expected filament deformation.

While the proposed methodology provides a robust and relevant framework for evaluating 3D-printing materials, several open problems still remain to be fully solved. The methodology still has limited ability to quantify actual filament deformation, as no standardized metrics exist to evaluate dimensional stability, layer compaction, or shape retention over time. Consequently, deformation was assessed qualitatively and cannot yet be directly linked to rheology or PFEM predictions. The rheological protocol also has an upper stress limit, with LC3 systems reaching maximum static yield stress within 1 h, restricting long-term monitoring. Simulations were conducted under simplified geometries and loading conditions, so they do not capture all process-level complexities, and experimental printing was performed at laboratory scale, leaving scalability to larger structures to be verified. The model is indeed capable of simulating more advanced behaviour, but the present study was specifically intended to provide a preliminary pathway for validating the printability of the mixtures. Increasing levels of complexity can be introduced once a formulation is selected and the geometry and scale of the printed object are clearly defined, including the type of information required from the simulation (e.g., layer shape evolution, interpenetration in complex toolpaths, buildability limits, etc.) [70].

5. Conclusions

In this study, six mortars incorporating ceramic wastes as a replacement of calcined clay in LC3 compositions were produced and rheologically characterized to evaluate their potential application in additive manufacturing. The aim was from one side to provide formulations with a reduced embodied CO_2 footprint of more than 40 % in comparison to PC, and on the other side to demonstrate their suitability as SCM for 3D printing applications. Raw materials characterization focused on SSA and SPV as key parameter to understand workability of mixtures. Rheological measurements were conducted by developing a specifically designed sequence for the application of a spherical probe rotating in a cylindrical cell. Numerical simulations with two different 3D-prinitng setups and with the rheological parameters identified as above finally enabled the prediction of the printability of the materials according to simplified patterns, further validated through an experimental proof of concepts. Based on the results the main innovative contributions of the work can be summarized as follows:

1. Ceramic waste powders were successfully used as replacements for calcined clay, demonstrating their potential as low-carbon raw materials in cementitious composites, with improved rheological effect on fresh mortar and further lowering embodied CO_2 footprint.
2. The ball measuring system with a specifically designed sequence proved to be a valuable tool for investigating mortars designed for three-dimensional printing, as it enables reliable measurements even in the presence of aggregates and at high static yield stress levels (kPa). The application of a rheological model allowed yield stress values to be quantified directly from flow table tests and provided an estimation of the thixotropy constant, thereby linking empirical and fundamental rheological assessments.
3. Numerical simulations highlighted that, while all tested formulations showed good performance for small-scale three-dimensional printing, careful material selection becomes crucial when targeting larger structures to ensure stability and minimize deformation. The preliminary 3D printing tests confirmed that the nozzle size and layer height are critical parameters in ensuring stable extrusion, adequate filament deposition, and consistent deformation resistance across different LC3-based mixtures.

Together, these results establish a framework that combines waste valorisation, advanced rheological testing, numerical modelling and 3D printing application to evaluate the suitability of novel cementitious materials for digital fabrication, advancing both sustainability and innovation in construction. It is worth highlighting that numerical simulation not only drastically reduces the need for countless experimental trials but also offers a powerful strategy for managing waste streams with compositions that fluctuate over time. By uniting rheology, modelling and printing trials, this work delivers a powerful route to rapidly optimise fresh-state behaviour and ensure robust 3D-printing

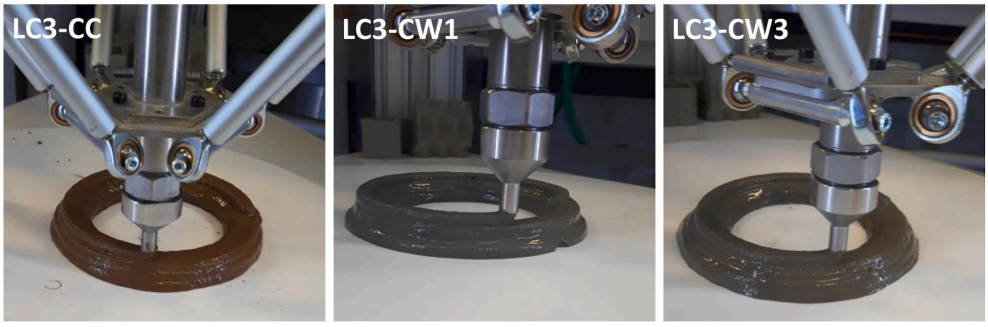

Fig. 11. Pictures of the 3D printing tests on a selection of analaysed materials used to validate the numerical simulation. From left to righ, LC3-CC, LC3-CW1 and LC3-CW3.

performance.

CRediT authorship contribution statement

Lucia Ferrari: Writing – review & editing, Writing – original draft, Methodology, Investigation, Formal analysis, Data curation, Conceptualization. **Giacomo Rizzieri:** Writing – review & editing, Software, Formal analysis, Data curation. **Liberato Ferrara:** Writing – review & editing, Visualization, Supervision, Conceptualization. **Elisa Franzoni:** Writing – review & editing, Supervision, Resources, Investigation, Funding acquisition, Conceptualization.

Declaration of competing interest

The authors declare that they have no known competing financial interests or personal relationships that could have appeared to influence the work reported in this paper.

Acknowledgment

This research was funded by the THIS. study was carried out within the MICS (Made in Italy – Circular and Sustainable) Extended Partnership and received funding from the European Union Next-Generation EU (PIANO NAZIONALE DI RIPRESA E RESILIENZA (PNRR) – MISSIONE 4 COMPONENTE 2, INVESTIMENTO 1.3 – D.D. 1551.11-10-2022, PE00000004). The second author acknowledges support from the project "Material and Process Modelling for Lunar 3D Printing", CUP D47G25000060006, funded under Notice No. 47 of February 20, 2025 ("Decree for the recruitment of international post-doctoral researchers"), PNRR Mission 4, Component 2, Investment 1.2, financed by the European Union – NextGeneration EU. Andrea Sgaravatto from University of Bologna is warmly thanked for their support during laboratory tests. Riccardo Pascolo from Centro Ceramico is thanked for providing the chemical analysis of ceramic wastes.

Appendix A. Supplementary data

Supplementary data to this article can be found online at https://doi.org/10.1016/j.cemconcomp.2025.106452.

Data availability

Data will be made available on request.

References

[1] I.-I.E.A. Wbcsd, Technology roadmap - low-carbon transition in the cement industry [Online]. Available: www.wbcsdcement.org, 2009.
[2] I.H. Shah, S.A. Miller, D. Jiang, R.J. Myers, Cement substitution with secondary materials can reduce annual global CO2 emissions by up to 1.3 gigatons, Nat. Commun. 13 (1) (Dec. 2022), https://doi.org/10.1038/s41467-022-33289-7.
[3] J. Skibsted, R. Snellings, Reactivity of supplementary cementitious materials (SCMs) in cement blends, Cement Concr. Res. 124 (Oct. 2019) 105799, https://doi.org/10.1016/J.CEMCONRES.2019.105799.
[4] M.C.G. Juenger, R. Snellings, S.A. Bernal, Supplementary cementitious materials: new sources, characterization, and performance insights, Cement Concr. Res. 122 (Aug. 2019) 257–273, https://doi.org/10.1016/J.CEMCONRES.2019.05.008.
[5] M. Zajac, J. Skocek, J. Skibsted, M. Ben Haha, Co2 mineralization of demolished concrete wastes into a supplementary cementitious material – a new ccu approach for the cement industry, RILEM Technical Letters 6 (Mar. 2021) 53–60, https://doi.org/10.21809/rilemtechlett.2021.141.
[6] M. Davolio, G. Muciaccia, L. Ferrara, Concrete Carbon Mixing – a Systematic Review on the Processes and Their Effects on the Material Performance, Elsevier Ltd., Mar. 01, 2025, https://doi.org/10.1016/j.clema.2025.100292.
[7] K. Scrivener, et al., Impacting factors and properties of limestone calcined clay cements (LC3), Green Mater. 7 (1) (Jul. 2018) 3–14, https://doi.org/10.1680/jgrma.18.00029.
[8] F. Zunino, K. Scrivener, Increasing the kaolinite content of raw clays using particle classification techniques for use as supplementary cementitious materials, Constr. Build. Mater. 244 (May 2020), https://doi.org/10.1016/j.conbuildmat.2020.118335.
[9] F. Zunino, K. Scrivener, The reaction between metakaolin and limestone and its effect in porosity refinement and mechanical properties, Cement Concr. Res. 140 (Feb) (2021), https://doi.org/10.1016/j.cemconres.2020.106307.
[10] Y. Dhandapani, et al., Durability performance of binary and ternary blended cementitious systems with calcined clay: a RILEM TC 282 CCL review, Materials and Structures/Materiaux et Constructions 55 (5) (Jun. 2022), https://doi.org/10.1617/s11527-022-01974-0.
[11] Z. Shi, et al., Durability of Portland Cement Blends Including Calcined Clay and Limestone: Interactions with Sulfate, Chloride and Carbonate Ions, 10, RILEM Bookseries, 2015, pp. 133–141, https://doi.org/10.1007/978-94-017-9939-3_17.
[12] M. Saillio, V. Baroghel-Bouny, S. Pradelle, Various durability aspects of calcined kaolin-blended Portland cement pastes and concretes, RILEM Bookseries 10 (2015) 491–499, https://doi.org/10.1007/978-94-017-9939-3_61.
[13] E. Roziere, G. Medjigbodo, L. Izoret, A. Loukili, Hydration and durability of ternary binders based on metakaolin and Limestone filler, RILEM Bookseries 25 (2020) 673–681, https://doi.org/10.1007/978-981-15-2806-4_75. Springer.
[14] A. Jan, L. Ferrari, N. Mikanovic, M. Ben-Haha, E. Franzoni, Chloride ingress and carbonation assessment of mortars prepared with recycled sand and calcined clay-based cement, Constr. Build. Mater. 456 (Dec) (2024), https://doi.org/10.1016/j.conbuildmat.2024.139337.
[15] A. Jan, L. Ferrari, V. Bortolotti, N. Mikanovic, M. Ben-Haha, E. Franzoni, Enhancement of mortar's properties by combining recycled sand and limestone calcined clay cement, Constr. Build. Mater. 442 (Sep. 2024) 137591, https://doi.org/10.1016/J.CONBUILDMAT.2024.137591.
[16] A.E. Lavat, M.A. Trezza, M. Poggi, Characterization of ceramic roof tile wastes as pozzolanic admixture, Waste Manag. 29 (5) (May 2009) 1666–1674, https://doi.org/10.1016/j.wasman.2008.10.019.
[17] P.C. Jacoby, F. Pelisser, Pozzolanic effect of porcelain polishing residue in Portland cement, J. Clean. Prod. 100 (Aug. 2015) 84–88, https://doi.org/10.1016/J.JCLEPRO.2015.03.096.
[18] F.J. García-Ten, M.F. Quereda Vázquez, C. Gil Albalat, D. Chumillas Villalba, V. Zaera, M.C. Segura Mestre, LIFE CERAM. Zero waste in ceramic tile manufacture, in: Key Engineering Materials, Trans Tech Publications Ltd, 2016, pp. 23–33, https://doi.org/10.4028/www.scientific.net/KEM.663.23.
[19] Confindustria Ceramica, L'Individuazione Dei Sottoprodotti Nelle Imprese Ceramiche Scarti Crudi E Scarti Cotti, 2017.
[20] L.A. Pereira-De-Oliveira, J.P. Castro-Gomes, P.M.S. Santos, The potential pozzolanic activity of glass and red-clay ceramic waste as cement mortars components, Constr. Build. Mater. 31 (Jun. 2012) 197–203, https://doi.org/10.1016/J.CONBUILDMAT.2011.12.110.
[21] E. Dos, et al., Materials Clay Ceramic Waste as Pozzolan Constituent in Cement for Structural Concrete, 2021, https://doi.org/10.3390/ma14112917.
[22] P.R. de Matos, et al., Utilization of ceramic tile demolition waste as supplementary cementitious material: an early-age investigation, J. Build. Eng. 38 (Jun) (2021), https://doi.org/10.1016/j.jobe.2021.102187.
[23] T.R. Muzenda, P. Hou, S. Kawashima, T. Sui, X. Cheng, The role of limestone and calcined clay on the rheological properties of LC3, Cem. Concr. Compos. 107 (Mar) (2020), https://doi.org/10.1016/j.cemconcomp.2020.103516.
[24] R. Li, L. Lei, J. Plank, Influence of PCE superplasticizers on the fresh properties of low carbon cements containing calcined clays: a comparative study of calcined clays from three different sources, Cem. Concr. Compos. 139 (May 2023), https://doi.org/10.1016/j.cemconcomp.2023.105072.
[25] M. Schmid, J. Plank, Interaction of individual Meta clays with polycarboxylate (PCE) superplasticizers in cement investigated via dispersion, zeta potential and sorption measurements, Appl. Clay Sci. 207 (Jun) (2021), https://doi.org/10.1016/j.clay.2021.106092.
[26] R. Sposito, M. Maier, N. Beuntner, K.C. Thienel, Evaluation of zeta potential of calcined clays and time-dependent flowability of blended cements with customized polycarboxylate-based superplasticizers, Constr. Build. Mater. 308 (Nov) (2021), https://doi.org/10.1016/j.conbuildmat.2021.125061.
[27] P. Boustingorry, Free superplasticizer concentration is a key influencer of the instantaneous thixotropy rates of cementitious pastes, Cement Concr. Res. 199 (Jan. 2026), https://doi.org/10.1016/j.cemconres.2025.108033.
[28] S. Dhers, et al., On the relationship between superplasticizer demand and specific surface area of calcined clays in LC3 systems, Constr. Build. Mater. 411 (Jan. 2024) 134467, https://doi.org/10.1016/J.CONBUILDMAT.2023.134467.
[29] L. Ferrari, V. Bortolotti, N. Mikanovic, M. Ben-Haha, E. Franzoni, Influence of calcined clay on workability of mortars with low-carbon cement, Journal, NanoWorld 9 (S2) (Sep. 2023) S30–S34, https://doi.org/10.17756/nwj.2023-s2-006.
[30] L. Ferrari, et al., Disclosing the mechanism behind rheological challenges in calcined clay-based cements, Constr. Build. Mater. 492 (Sep. 2025) 142837, https://doi.org/10.1016/j.conbuildmat.2025.142837.
[31] L. Ferrari, V. Bortolotti, N. Mikanovic, M. Ben-Haha, E. Franzoni, Understanding workability of low carbon cements through advanced water detection techniques, Sci. Rep. 15 (1) (Oct. 2025) 35112, https://doi.org/10.1038/s41598-025-19203-3.
[32] N. Roussel, Rheological Requirements for Printable Concretes, Elsevier Ltd., Oct. 01, 2018, https://doi.org/10.1016/j.cemconres.2018.04.005.
[33] R. Nicolas, et al., Assessing the fresh properties of printable cement-based materials: high potential tests for quality control, Cement Concr. Res. 158 (Aug. 2022), https://doi.org/10.1016/j.cemconres.2022.106836.
[34] F. Bos, R. Wolfs, Z. Ahmed, T. Salet, Additive manufacturing of concrete in construction: potentials and challenges of 3D concrete printing, Virtual Phys. Prototyp. 11 (3) (Jul. 2016) 209–225, https://doi.org/10.1080/17452759.2016.1209867.

[35] R. J. M. Wolfs and A S J Suiker, "Structural failure during extrusion-based 3D printing processes," Int. J. Adv. Manuf. Technol., doi: 10.1007/s00170-019-03844-6.
[36] N. Roussel, H. Bessaies-Bey, S. Kawashima, D. Marchon, K. Vasilic, R. Wolfs, Recent advances on yield stress and elasticity of fresh cement-based materials, Cement Concr. Res. 124 (Oct. 2019) 105798, https://doi.org/10.1016/J.CEMCONRES.2019.105798.
[37] R.J.M. Wolfs, F.P. Bos, T.A.M. Salet, Early age mechanical behaviour of 3D printed concrete: numerical modelling and experimental testing, Cement Concr. Res. 106 (Apr. 2018) 103–116, https://doi.org/10.1016/J.CEMCONRES.2018.02.001.
[38] T. Ooms, G. Vantyghem, R. Van Coile, W. De Corte, A parametric modelling strategy for the numerical simulation of 3D concrete printing with complex geometries, Addit. Manuf. 38 (Feb) (2021), https://doi.org/10.1016/j.addma.2020.101743.
[39] R. Comminal, W.R. Leal da Silva, T.J. Andersen, H. Stang, J. Spangenberg, Modelling of 3D concrete printing based on computational fluid dynamics, Cement Concr. Res. 138 (Dec. 2020), https://doi.org/10.1016/j.cemconres.2020.106256.
[40] G. Rizzieri, L. Ferrara, M. Cremonesi, Numerical simulation of the extrusion and layer deposition processes in 3D concrete printing with the Particle finite element method, Comput. Mech. 73 (2) (Feb. 2024) 277–295, https://doi.org/10.1007/s00466-023-02367-y.
[41] G. Rizzieri, S. Meni, M. Cremonesi, L. Ferrara, A particle finite element method for investigating the influence of material and process parameters in 3D Concrete printing, Comput. Struct. 316 (Sep) (2025), https://doi.org/10.1016/j.compstruc.2025.107883.
[42] R.J.M. Wolfs, T.A.M. Salet, N. Roussel, Filament geometry control in extrusion-based additive manufacturing of concrete: the good, the bad and the ugly, Cement Concr. Res. 150 (Dec. 2021), https://doi.org/10.1016/j.cemconres.2021.106615.
[43] R. Jayathilakage, P. Rajeev, J. Sanjayan, Rheometry for Concrete 3D Printing: a Review and an Experimental Comparison, MDPI, Aug. 01, 2022, https://doi.org/10.3390/buildings12081190.
[44] C. Zhang, et al., A two-phase design strategy based on the composite of mortar and coarse aggregate for 3D printable concrete with coarse aggregate, J. Build. Eng. 54 (Aug) (2022), https://doi.org/10.1016/j.jobe.2022.104672.
[45] H. F. W., F.W. Harry, Taylor, Cement Chemistry, second ed., Academic Press, 1990.
[46] L. Ferrari, E. Franzoni, Use OF ceramic wastes to develop low carbon cement for made in Italy industry, Environ Eng Manag J 24 (10) (2025) 2171–2179, https://doi.org/10.30638/eemj.2025.168.
[47] British Standards Institution, EN 197-6, Tests for Mechanical and Physical Properties of Aggregates. Part 6: Determination of Particle Density and Water Absorption, 2000. London.
[48] British Standards Institution, EN 196-1:2016, Methods of Testing Cement. Part 1, Determination of strength, London, 2016.
[49] J. Landers, G.Y. Gor, A.V. Neimark, Density functional theory methods for characterization of porous materials, Colloids Surf. A Physicochem. Eng. Asp. 437 (2013) 3–32, https://doi.org/10.1016/j.colsurfa.2013.01.007.
[50] ASTM International, ASTM C1437 − 20: Standard Test Method for Flow of Hydraulic Cement Mortar. doi: 10.1520/C1437.
[51] Y. Kurokawa, Y. Tanigawa, H. Mori, R. Komura, A Study on the Slump Test and Slump Flow Test of Fresh Concrete, 6, TRANSACTIONS OF THE JAPAN CONCRETE INSTITUTE, 1994.
[52] F. Soave, G. Muciaccia, L. Ferrara, An indirect methodology to evaluate the rheological properties of a digitally fabricated concrete incorporating corrosion inhibitors, in: Proceedings of the RILEM Spring Convention and Conference 2024. RSCC 2024, RILEM Bookseries, 2025, pp. 301–309, https://doi.org/10.1007/978-3-031-70281-5_34.
[53] N. Roussel, P. Coussot, Fifty-cent rheometer' for yield stress measurements: from slump to spreading flow, J. Rheol. 49 (3) (May 2005) 705–718, https://doi.org/10.1122/1.1879041.
[54] M. Schatzmann, G.R. Bezzola, H.E. Minor, E.J. Windhab, P. Fischer, Rheometry for large-particulated fluids: analysis of the ball measuring system and comparison to debris flow rheometry, Rheol. Acta 48 (7) (2009) 715–733, https://doi.org/10.1007/s00397-009-0364-x.
[55] Y. Qian, S. Kawashima, Distinguishing dynamic and static yield stress of fresh cement mortars through thixotropy, Cem. Concr. Compos. 86 (Feb. 2018) 288–296, https://doi.org/10.1016/j.cemconcomp.2017.11.019.
[56] P. V Liddell, D. V Boger, Yield Stress Measurements with the Vane, 1996.
[57] N. Roussel, A thixotropy model for fresh fluid concretes: theory, validation and applications, Cement Concr. Res. 36 (10) (Oct. 2006) 1797–1806, https://doi.org/10.1016/j.cemconres.2006.05.025.
[58] M. Cremonesi, A. Franci, S. Idelsohn, E. Oñate, A state of the art review of the Particle finite element Method (PFEM), Arch. Comput. Methods Eng. 27 (5) (Nov. 2020) 1709–1735, https://doi.org/10.1007/s11831-020-09468-4.
[59] H. Edelsbrunner, E. Mucke, Three dimensional alpha shapes, ACM Trans. Graph. 13 (1) (Jan. 1994) 43–72.
[60] G. Rizzieri, M. Cremonesi, L. Ferrara, A 2D numerical model of 3D concrete printing including thixotropy, Mater. Today Proc. (Aug. 2023), https://doi.org/10.1016/j.matpr.2023.08.082.
[61] G. Rizzieri, L. Ferrara, M. Cremonesi, Simulation of viscoelastic free-surface flows with the particle finite Element method, Comput. Times Part Mech (Oct. 2024), https://doi.org/10.1007/s40571-024-00730-1.
[62] G. Rizzieri, L. Ferrara, M. Cremonesi, A partitioned Lagrangian finite element approach for the simulation of viscoelastic and elasto-viscoplastic free-surface flows, Comput. Methods Appl. Mech. Eng. 443 (Aug) (2025), https://doi.org/10.1016/j.cma.2025.118071.
[63] T.C. Papanastasiou, Flows of materials with yield, J. Rheol. 31 (5) (Jul. 1987) 385–404, https://doi.org/10.1122/1.549926.
[64] P. Carneau, R. Mesnil, O. Baverel, N. Roussel, Layer pressing in concrete extrusion-based 3D-printing: experiments and analysis, Cement Concr. Res. 155 (May 2022), https://doi.org/10.1016/j.cemconres.2022.106741.
[65] M. Thommes, et al., Physisorption of gases, with special reference to the evaluation of surface area and pore size distribution (IUPAC Technical report), Pure Appl. Chem. 87 (9–10) (Oct. 2015) 1051–1069, https://doi.org/10.1515/pac-2014-1117.
[66] S. Moghul, F. Zunino, R.J. Flatt, Flow loss in superplasticized limestone calcined clay cement, J. Am. Ceram. Soc. 108 (5) (May 2025), https://doi.org/10.1111/jace.20344.
[67] R.J. Flatt, N. Roussel, H. Bessaies-Bey, L. Caneda-Martínez, M. Palacios, F. Zunino, From physics to chemistry of fresh blended cements, Cement Concr. Res. 172 (Oct. 2023), https://doi.org/10.1016/j.cemconres.2023.107243.
[68] S. Mantellato, M. Palacios, R.J. Flatt, Impact of sample preparation on the specific surface area of synthetic ettringite, Cement Concr. Res. 86 (Aug. 2016) 20–28, https://doi.org/10.1016/j.cemconres.2016.04.005.
[69] L. Ferrari, P. Boustingorry, The Influence of Paste Thixotropy on the Formwork-Filling Properties of Concrete, American Concrete Institute, ACI Special Publication 11th International Conference on Superplasticizers and Other Chemical Admixtures in Concrete Ottawa, 2015, pp. 449–462, https://doi.org/10.14359/51688116, 2015-January, no. SP 302.
[70] G. Rizzieri, M. Cremonesi, L. Ferrara, Challenging the limits of fluid FEM modelling in 3D concrete printing, RILEM Bookseries 53 (2024) 482–489, https://doi.org/10.1007/978-3-031-70031-6_56. Springer Science and Business Media B.V.